Investigation of unsteady separation using novel back-illuminated temperature sensitive paint setup and near wall Lagrangian particle tracking

M. Hilfer[1], R. Braun[1], T. K. Lindner[1], M. Mendler[1], D. E. Rival [1]

1: Institute of Fluid Mechanics, TU Braunschweig, Germany
*Corresponding author: michael.hilfer@tu-braunschweig.de

Keywords: Back-illuminated temperature-sensitive paint, TSP, Lagrangian particle tracking, time-resolved measurements.

ABSTRACT

This study presents an experimental investigation into the detection and analysis of unsteady flow separation on a cylinder in cross-flow at a subcritical Reynolds number of $Re_D = 1.9 \times 10^5$. The methodology combines a novel model-integrated, back-illuminated temperature-sensitive paint (TSP) system with simultaneous near-wall Lagrangian particle tracking and external volumetric three-dimensional particle tracking velocimetry (3D-PTV). Although traditional Eulerian criteria (such as vanishing wall shear stress) are widely applied, they exhibit significant physical limitations in unsteady flow regimes. Consequently, time-resolved spatial and Lagrangian analyses provide a more robust, frame-independent approach to characterizing fluid separation. To achieve this, a specialized transparent experimental setup was developed, internally housing all optical components and utilizing a transparent conductive heating layer. This inside-out configuration permits continuous surface thermography without obstructing the external flow field. The acquired optical data is mathematically decomposed using Robust Principal Component Analysis (RPCA) to effectively isolate the near-wall tracer kinematics from the underlying low-rank thermodynamic footprint. Furthermore, Spectral Proper Orthogonal Decomposition (SPOD) is applied to identify the dominant spectral frequencies governing the separation dynamics. By successfully fusing the time-resolved volumetric particle tracks with the transient TSP surface fields, this study provides unambiguous experimental evidence of near-wall reverse flow and discrete Lagrangian fluid ejection events. The established methodology forms the requisite foundation for future extractions of instantaneous wall-shear-stress fields, ultimately aiming to experimentally validate the Lagrangian Repulsion Rate separation criterion.

1. Introduction

The study of fluid dynamics has historically been divided into two distinct observational frameworks: the Eulerian perspective, which observes flow properties at fixed spatial coordinates, and the Lagrangian perspective, which tracks the trajectory and history of individual fluid parcels. While the Eulerian approach has dominated engineering applications due to its compatibility with fixed sensors and steady-state analysis, it proves insufficient for the complex, unsteady flows inherent to modern aerodynamic challenges. For over a century, the detection of flow separation has relied on the boundary layer theory established by Prandtl in 1904. In the context of a two-dimensional, steady flow over a fixed wall, separation is defined as the point where the boundary layer detaches from the surface, creating a wake. Mathematically, this is identified as the location where the wall shear stress (τ_w) vanishes:

$$\tau_w = \mu \left(\frac{\partial u}{\partial y} \right)_{y=0} = 0 \tag{1}$$

where μ is the dynamic viscosity, u is the streamwise velocity, and y is the coordinate normal to the wall. This condition is typically accompanied by a singular behavior in the boundary layer equations and the onset of flow reversal.

However, contemporary literature highlights that this definition breaks down in unsteady flows. In a time-dependent field, the point of zero skin friction ($\tau_w = 0$) moves along the wall. A fluid particle experiencing zero shear stress at one instant may essentially "ride" the moving point of zero shear without ever detaching from the wall. Conversely, separation—physically understood as the ejection of vorticity and mass into the free stream—can occur at locations where the shear stress is non-zero. This phenomenon, formalized by the Moore-Rott-Sears (MRS) criterion Sears & Telionis (1975), suggests that separation in unsteady flows occurs at a point of vanishing shear within a frame of reference moving with the separation structure, not the wall frame. This discrepancy necessitates a shift to the Lagrangian perspective, which defines separation based on the asymptotic behavior of fluid particles rather than instantaneous local snapshots.

To resolve the ambiguities of the Eulerian framework, this work highlights a Lagrangian approach: the Repulsion Rate criterion Sadr & Vétel (2024). Rooted in the theory of Lagrangian Coherent Structures (LCS) Haller (2015), the repulsion rate specifically examines hyperbolic structures that act as transport barriers. Consider a material surface advected by the flow. The repulsion rate, ρ, quantifies the exponential rate at which infinitesimal perturbations normal to this surface grow. In the context of flow separation, a separating stream surface acts as a repeller: fluid particles approaching it are forced to diverge rapidly, either remaining in the boundary layer or being ejected into the wake. Consequently, the "Lagrangian separation point" is defined as the location on the wall where this normal repulsion is maximized.

Sadr and Vétel (2024) derived a direct link between this Lagrangian quantity and measurable Eulerian wall properties. For an incompressible flow over a rigid no-slip boundary, they demonstrated that the rate of change of the repulsion rate, $\dot{\rho}$, is given by the second wall-normal derivative of the

wall-normal velocity component, evaluated at the wall:

$$\dot{\rho} = \left(\frac{\partial^2 v}{\partial y^2}\right)_{\text{wall}} \tag{2}$$

Using the continuity equation ($\nabla \cdot \mathbf{u} = 0$) and the definition of the wall shear stress vector $\boldsymbol{\tau}_w = (\tau_x, \tau_z)$, this expression can be rewritten in terms of the divergence of the skin friction field:

$$\left(\frac{\partial^2 v}{\partial y^2}\right)_{\text{wall}} = -\frac{1}{\mu}\nabla \cdot \boldsymbol{\tau}_w = -\frac{1}{\mu}\left(\frac{\partial \tau_x}{\partial x} + \frac{\partial \tau_z}{\partial z}\right) \tag{3}$$

This derivation is pivotal, as it provides a theoretical bridge between an abstract Lagrangian concept and the experimental capabilities of Temperature-Sensitive Paint (TSP) Miozzi et al. (2016); Liu et al. (2021).

To investigate this Lagrangian criterion experimentally, this research utilizes TSP, a molecular sensor that converts surface temperature into luminescent intensity. The paint consists of active probe molecules (luminophores) immobilized in a polymer matrix. Upon excitation by a photon of appropriate energy, a luminophore molecule transitions to an excited singlet state. The return to the ground state occurs via radiative decay (phosphorescence/fluorescence) or temperature-dependent non-radiative decay (thermal quenching). The quantum efficiency Φ is the ratio of the radiative decay rate (k_r) to the total decay rate (radiative plus non-radiative, k_{nr}):

$$\Phi = \frac{k_r}{k_r + k_{nr}(T)} \tag{4}$$

Because the non-radiative rate k_{nr} is strongly temperature-dependent, an increase in temperature increases the probability of thermal quenching, thereby reducing the emission intensity. This work employs a normalized intensity ratio approach to account for non-uniform illumination:

$$\frac{I(T)}{I(T_{\text{ref}})} = F\left(\frac{T}{T_{\text{ref}}}\right) \tag{5}$$

where I is the emission intensity and T_{ref} is a known reference temperature. The specific TSP used in this work utilizes a Ruthenium complex (Ru(phen)), chosen for its high quantum yield, large Stokes shift, suitable temperature sensitivity (typically 1–4% per Kelvin), and an excitation wavelength within the visible spectrum (e.g., 460 nm).

While TSP provides spatially and temporally resolved temperature maps ($T_w(x, z, t)$), the Lagrangian analysis requires the wall shear stress vector $\boldsymbol{\tau}_w$. The optical flow (OF) method Horn & Schunck (1981) bridges this gap by exploiting the Reynolds analogy—the similarity between momentum and heat transfer in the viscous sublayer. Pioneered for this application by Liu et al. Liu & Woodiga (2011), the method begins with the unsteady energy equation for an incompressible fluid at the wall. Within the viscous sublayer ($y^+ < 5$), convection and diffusion dominate. By performing a Taylor series expansion of velocity and temperature normal to the wall:

$$u \approx \frac{\tau_x}{\mu} y, \quad w \approx \frac{\tau_z}{\mu} y, \quad T \approx T_w + \frac{q_w}{k} y \tag{6}$$

and substituting these into the energy equation in the limit as $y \to 0$, the fundamental optical flow equation for near-wall transport is obtained:

$$F + \tau_x \frac{\partial T_w}{\partial x} + \tau_z \frac{\partial T_w}{\partial z} = 0 \tag{7}$$

Here, F is a source term encapsulating the thermal inertia of the fluid and the unsteady heat flux at the wall:

$$F \propto \frac{\partial q_w}{\partial t} - \alpha_{\text{th}} \nabla^2 q_w \tag{8}$$

where q_w is the wall heat flux and α_{th} is the thermal diffusivity. The measurable surface temperature gradient, ∇T_w, thus links the TSP measurements directly to the repulsion rate separation criterion proposed by Sadr and Vétel.

Figure 1, adapted from Serra et al. (2018), illustrates schematically the fluid kinematics and a qualitative surface temperature distribution in the vicinity of an unsteady separation region. In this schematic, the classical Eulerian separation point, defined by Prandtl as the locus of vanishing wall shear stress, is denoted by the green marker, p. In contrast, the Lagrangian separation topology is characterized by a repelling material manifold, represented by the solid red line, which originates at the true Lagrangian separation point on the wall, s_p. The orange tracer particles demonstrate the physical mechanism of this process: as they are advected through the near-wall flow field, they experience a Lagrangian repulsion event. These fluid parcels are forced to detach from the surface with varying wall-normal velocities, ultimately converging onto and riding along the repelling manifold into the wake. By tracking the instantaneous spatial evolution of this material manifold and tracing it back to its root on the wall, the exact physical origin of the fluid ejection event can be localized, thereby identifying the Lagrangian separation point s_p.

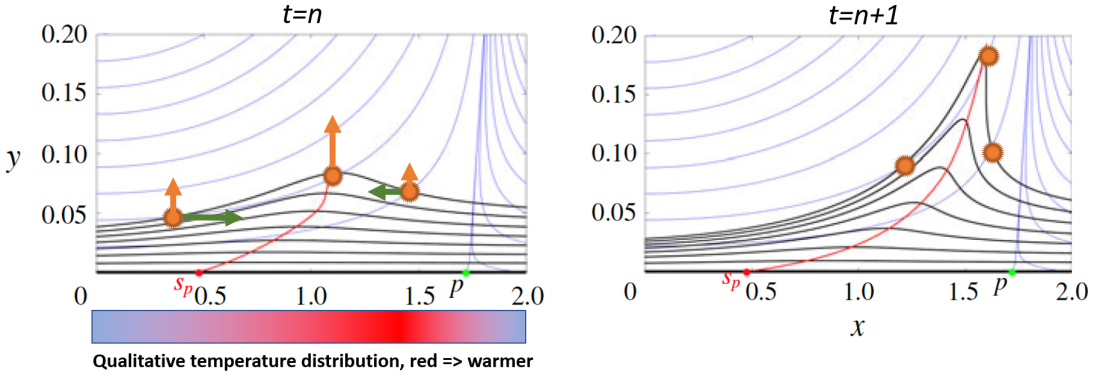


Figure 1. Modified from Serra et al. (2018). Showing the evolution of fluid material manifold and fluid parcels in orange overlaid on top of stream lines. In red - Lagrangian separation point S_p and in green the Prandtl separation point P are shown along with qualitative temperature distribution on the surface.

Although the extraction of unsteady temperature fields from TSP is an established technique, simultaneously linking near-wall flow dynamics to global surface temperature data remains a significant experimental challenge. The novelty of this work lies in directly connecting temporally

and spatially resolved TSP temperature maps to the unsteady, three-dimensional flow structures separating above the surface. By combining these measurement techniques with Lagrangian flow theory, this study aims to isolate the precise behavior of fluid particles within the separation region.

To capture the coupled dynamics of the fluid-solid interface without optical interference, a novel back-illuminated Temperature-Sensitive Paint (TSP) configuration is introduced. Traditionally, TSP excitation and emission capture share the same optical path as the flow field measurement, often leading to restricted optical access and problematic signal cross-talk with laser illumination. By utilizing an optically transparent model, the TSP layer applied to the wetted surface can be excited, and its luminescent emission recorded, entirely from behind the structure. This configuration leaves the flow-facing geometry completely unobstructed, a prerequisite for simultaneous, high-resolution optical flow diagnostics.

The flow field kinematics are subsequently extracted through two simultaneous, complementary data analysis modalities. First, the two-dimensional, surface-bound flow topology is derived directly from the unsteady TSP images. By applying the optical flow (OF) methodology to these temporally resolved temperature maps, the continuous skin friction field (τ_w) can be extracted. This provides the necessary foundation for evaluating the Lagrangian repulsion rate at the wall. Second, the off-surface, three-dimensional flow field is captured concurrently using Shake-The-Box (STB). As an advanced Lagrangian particle tracking velocimetry technique, STB yields highly resolved, volumetric particle trajectories, mapping the time-resolved velocity and acceleration fields within the boundary layer and the free stream. Furthermore, this dataset enables the evaluation of whether temporally evolving surface temperature fields alone are sufficient to capture Lagrangian repulsion events. As an additional benefit of this configuration, a third dataset is extracted by utilizing the internal TSP imaging system to track fluid particles situated close to the wall.

The core methodological advancement of this setup lies in the spatial and temporal synthesis of these three independent datasets. The surface coordinate system of the TSP data is precisely calibrated and mapped to the volumetric domain of the STB measurements. Establishing this bridge enables the continuous wall topology, once extracted, to be mathematically linked to the discrete Lagrangian particle tracks. This simultaneous linkage would allow us for a direct correlation between localized surface signatures, such as the loci of maximum repulsion, and the physical ejection or advection of three-dimensional vortical structures into the wake.

2. Experimental Methods

The experimental setup comprises two distinct, synchronized measurement systems: an internal configuration designed for back-illuminated temperature-sensitive paint (TSP) thermography combined with concurrent near-wall particle tracking, and an external arrangement dedicated to volumetric three-dimensional particle tracking velocimetry (3D-PTV) of the surrounding flow field. The temporal synchronization of both subsystems is regulated by a master function generator. To adequately resolve the higher frequency dynamics of the off-surface flow, the external

high-speed cameras are operated at an integer multiple of the internal camera's frame rate.

The experiments are conducted in the large water tunnel (GWB) at the Technical University of Braunschweig, utilizing a physical model constructed from a transparent acrylic (PMMA) cylinder. This material was selected due to its excellent optical transmittance in the visible spectrum combined with favorable mechanical machinability. The cylinder features an outer diameter of $D = 150\,\mathrm{mm}$ and spans the full width of the water tunnel test section, as illustrated in Fig. 2a. This specific diameter ensures sufficient internal volume to house the optical instrumentation while keeping the tunnel blockage ratio at a manageable $15\,\%$. The Reynolds numbers investigated in the experiments to date range between $Re_D = 1.9 \times 10^5$ and $Re_D = 6.8 \times 10^5$, utilizing the cylinder diameter as the characteristic length scale. This operational range spans from subcritical conditions, characterized by a purely laminar separation and a pronounced vortex sheet, up to the immediate vicinity of supercritical conditions, where a mixed laminar-turbulent transition shifts the separation line further downstream.

2.1. External Setup

The external diagnostic suite primarily comprises four high-speed cameras (Phantom T4040 and T2540) operating at a sensor resolution of 2560×1664 pixels ($16.05\,\mu\mathrm{m\,px^{-1}}$ spatial resolution). This system is capable of achieving frame rates up to $5\,\mathrm{kHz}$ at full sensor resolution. The cameras are equipped with $50\,\mathrm{mm}$ Nikkor lenses set to an aperture of $f/8$. To ensure uniform focus across the depth of the measurement volume, Scheimpflug adapters are mounted between the camera bodies and the lenses. Notably, no optical filters are utilized on the external camera suite. The schematic on the right side of Fig. 2b details the target volume within which the 3D-PTV measurements are performed. To capture the generation and development of the transient wake in greater detail, the measurement volume is shifted slightly downstream relative to the cylinder axis. Two high-power pulsed LEDs (LaVision LED-Flashlight 300) are positioned on opposite sides of the water tunnel hull, illuminating the target volume at an angle opposing the primary fluid flow direction. The various measurement subsystems are synchronized using a LaVision Programmable Timing Unit (PTU) coupled with an external master frequency generator. Images acquired by the cameras are streamed to a high-performance workstation and post-processed using LaVision DaVis 11 software. The initial spatial calibration of the optical setup was performed using a standard LaVision 3D calibration target, followed by a volume self-calibration procedure utilizing the actual acquired particle images to correct for dynamic misalignments and refine the mapping function. Finally, polyamide particles with a nominal diameter of $100\,\mu\mathrm{m}$ are seeded into the tunnel to serve as fluid tracers.

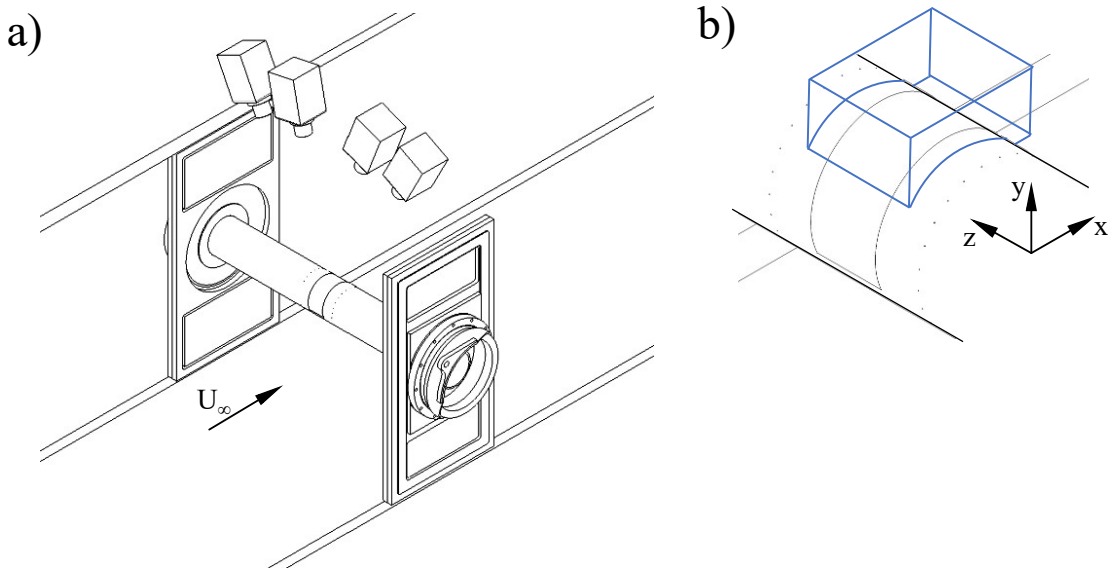


Figure 2. Overview of the external setup: a) position of the cylinder within the test section and the spatial arrangement of the high-speed cameras; b) schematic representation of the 3D-PTV measurement volume.

Although polyamide particles provide near-neutral buoyancy, the nominal diameter of $100\,\mu m$ introduces inherent hydrodynamic limitations in high-gradient flows. Specifically, the increased particle relaxation time limits the frequency response, reducing tracking fidelity within the high-frequency turbulent fluctuations of the separated wake. Furthermore, within the steep velocity gradients of the near-wall region, particles of this size are susceptible to spatial averaging and shear-induced lift forces, which can bias the Lagrangian trajectories away from true fluid pathlines. Despite these recognized drawbacks, this particle size was strictly necessitated by the optical and spatial resolution limits of the internal camera setup. The model-integrated sensor required the larger cross-sections of the $100\,\mu m$ tracers to achieve a sufficient signal-to-noise ratio for the inside-out tracking algorithm. In future investigations, planned refinements to the internal optical train will enable a reduction in tracer diameter to a more manageable $20\,\mu m$, which will significantly improve the temporal and spatial tracking response while maintaining optical visibility.

2.2. Internal Setup

The experimental centerpiece of this study is the model-integrated, inside-out (back-illuminated) optical measurement system (Fig. 3). Traditional TSP implementations in hydrodynamic or aerodynamic facilities rely on external cameras and excitation sources viewing the model through test-section windows. This conventional approach suffers from critical limitations: optical distortion from thick glass walls, restricted viewing angles, visual obstruction by model supports, susceptibility to structural vibrations, and particle shadowing during simultaneous surface and flow-field measurements. To circumvent these issues, the optical and illumination hardware required for TSP thermography are integrated directly inside the hollow cylinder model. Consequently, both the structural substrate and the integrated heating layer necessary to drive the TSP heat flux must

be entirely optically transparent.

The internal optical assembly features an industrial camera (IDS, uEye+ SE) equipped with a Sony IMX426, global shutter CMOS sensor operating at a resolution of up to 816 × 624 pixels and a frame rate of up to 1000 Hz. The camera is aligned with the longitudinal axis of the cylinder, as depicted in Fig. 3a. To accommodate the short working distance imposed by the internal radius, the camera utilizes a compact, fixed-focal-length industrial lens (Edmund Optics UC-series, $f = 8\,\mathrm{mm}$) set to an aperture of f/5.6. A long-pass optical filter (Thorlabs FGL570) is mounted ahead of the lens to isolate the luminescent emission of the TSP from the excitation light and external illumination sources. The entire camera module is secured to an internal rail system, permitting precise axial translation and circumferential rotation to target specific angular sectors of the cylinder surface.

Data acquisition is facilitated via a USB 3.0 interface connecting the camera to an external workstation, with cables routed through the cylinder's structural supports. The data from the internal camera is streamded to the workstation allowing for long duration acquisition. Importantly, the internal camera exposure is temporally synchronized with the external 3D-PTV system via the central LaVision Programmable Timing Unit (PTU), ensuring the surface thermography and volumetric kinematics are strictly phase-locked. Addtionally, due to phase-locking of the measurement, any parasitic light from the external system is compensated.

For TSP excitation, a high-power blue LED module (custom made with center wavelength $460\,\mathrm{nm}$–$470\,\mathrm{nm}$), equipped with an appropriate band-pass excitation filter ($430\,\mathrm{nm}$–$480\,\mathrm{nm}$), is integrated into the internal chassis. To enable the optical flow (OF) evaluation, the model surface is electrically heated to maintain a positive wall-to-fluid temperature gradient ($T_w > T_\infty$). Because the optical path traverses both the $8\,\mathrm{mm}$ thick PMMA cylinder wall and the heating element, the heater is engineered to be highly transparent, utilizing a conductive Indium Tin Oxide (ITO) coating. The applied uniform surface heat flux is $3.6\,\mathrm{kW\,m^{-2}}$, yielding Richardson numbers below $Ri = 1.55 \times 10^{-3}$. This confirms that buoyancy-driven natural convection is negligible and the boundary layer dynamics are entirely governed by the forced flow. Finally, a custom temperature-sensitive paint based on Ru(phen) luminophore was formulated specifically for this back-illuminated application and applied via airbrushing to a thickness of approximately 40 μm.

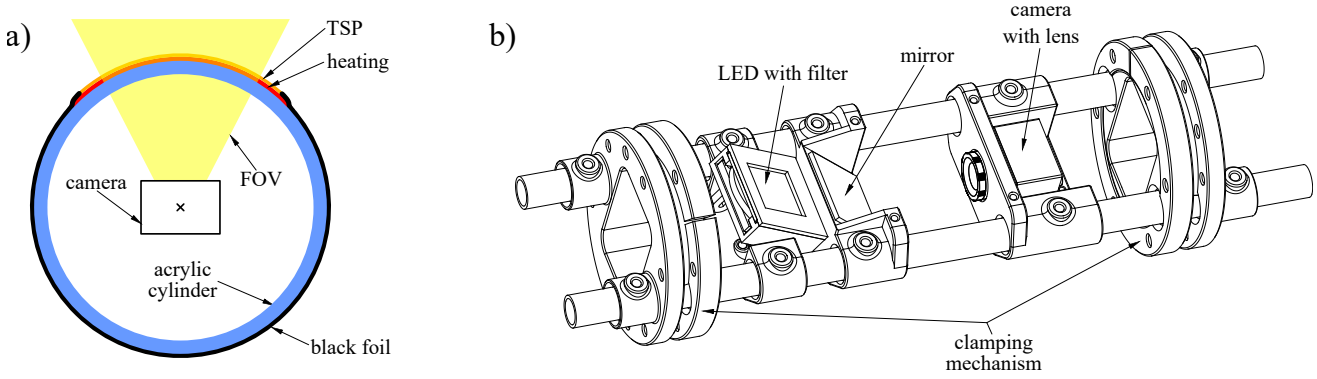


Figure 3. Overview of the internal setup: a) schematic cross-sectional view along the longitudinal axis of the cylinder; b) internal instrumentation chassis clamped securely inside the model.

This inside-out architecture inherently unifies two diagnostic modalities within a single optical train: surface TSP thermography and near-wall particle tracking. Both analyses are performed concurrently using the identical stream of filtered images acquired by the internal camera. The particle tracking methodology exploits the phenomenon that the luminescent TSP layer acts as a diffuse, homogeneous backlight, illuminating near-wall fluid tracers from behind. Assuming a uniform surface emission intensity, the captured luminescent footprint of a tracer particle is monotonically related to its wall-normal distance, as illustrated in Fig. 4. When coupled with a spatial two-dimensional calibration of the internal camera, this intensity modulation provides quantitative in-plane projected particle trajectories (x, z) and a qualitative history of the out-of-plane, wall-normal position (y) along each individual track.

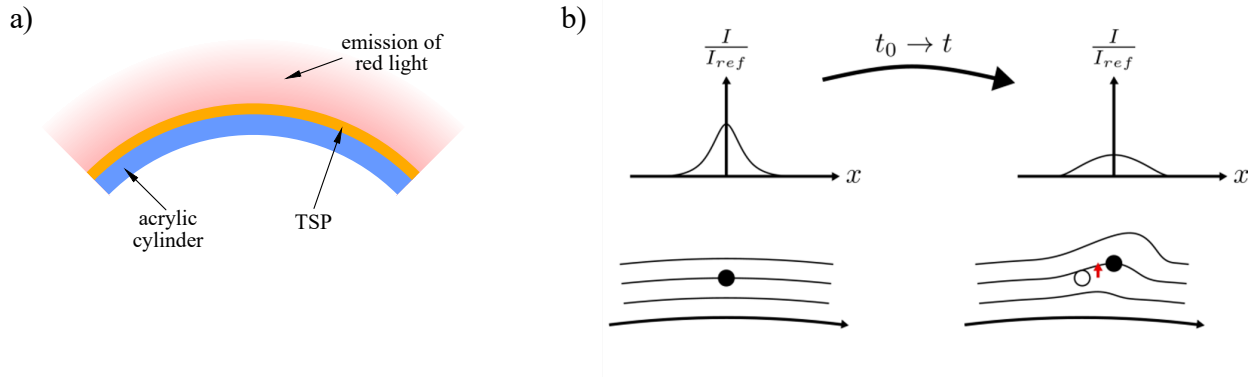


Figure 4. Inside-out tracking method: a) schematic diagram of the near-wall particle illumination by the active TSP layer; b) idealized intensity response of tracer particles as a function of wall-normal distance.

The image acquisition protocol for a single measurement point consists of four distinct phases:

1. **Dark images:** Acquired without illumination to assess the inherent dark current and noise characteristics of the internal camera sensor. These baseline images are subsequently subtracted from all reference and run images to improve the overall signal-to-noise ratio.

2. **Pre-run images:** Acquired prior to the experimental run with the internal heating deactivated. At lower Reynolds numbers, these are taken under low-speed conditions, whereas for higher Reynolds numbers, they are acquired at the target velocity. In the absence of active heating, the cylinder surface temperature is assumed to be spatially uniform and in thermal equilibrium with the freestream fluid. These images serve as the primary reference (I_{ref}) for calculating the surface temperature distribution.

3. **Run images:** Acquired under the target experimental conditions (the specified Reynolds number) with the internal surface heating actively engaged.

4. **Post-run images:** Acquired immediately following the run sequence with the heating deactivated. For both low and high Reynolds number measurements, the water tunnel velocity is reduced to a minimum during this phase. These images provide a secondary reference to

verify the thermal stability of the setup and account for any potential temperature drift or luminophore degradation that may have occurred during the run.

Complementing the internal optical setup, discrete resistance temperature detectors (Pt1000) are integrated directly into the cylinder wall to provide a simultaneous, in-situ calibration reference for the TSP measurements. These physical sensors are intentionally positioned within the field of view of the internal camera. Their temperature readings are acquired synchronously with the Pre-run, Run, and Post-run image sequences, enabling the precise conversion of normalized luminescent intensities into quantitative, absolute temperature fields.

3. Data Processing

The datasets acquired from the internal and external measurement systems are initially processed through independent computational pipelines before being spatially and temporally fused.

3.1. External Setup

A total volume with $160\,\mathrm{mm}$ in span, $110\,\mathrm{mm}$ in streamwise and $80\,\mathrm{mm}$ in vertical direction is observed with four cameras at $1.5\ kHz$. The raw images are preprocessed with a sliding minimum subtraction of 10 counts and a temporal sliding minimum subtraction over 11 snapshots. The in DaVis 11 implemented shake the box algorithm is used for particle reconstruction and tracking.

Calibrated images are aligned with surface markers visible in both internal and external camera views. A two channel function generator serves as the master clock for tracking and TSP images, ensuring temporal synchronization and a common trigger.

3.2. Internal Setup

A complete custom data acquisition and TSP post-processing tool with graphical user interface was realized for this and future measurements. It consists of following sub-modules which were also followed during post-processing of the datasets:

- **Data Acquisition:** This module, developed using the IDS SDK, features optimized memory allocation protocols to mitigate write-speed bottlenecks during image storage. Hardware-specific parameters (exposure, gain, frame rate, etc.) are applied via an IDS settings file ('.cset') during camera initialization. To guarantee zero frame drops, data is captured directly into pre-allocated memory buffers. The acquisition is divided into four distinct phases with configurable frame counts: Dark, Pre-run, Run, and Post-run images.
- **Data Export:** Post-acquisition, the image sequences are exported and stored as either 12-bit/16-bit TIFF files or serialized NumPy arrays for further computational analysis.

- **Noise Reduction:** This step analyzes the dark image phase to compute a temporally averaged master dark frame and characterize the temporal noise. It calculates the global offset and dark signal non-uniformity, and identifies dead or hot pixels using a dynamic thresholding algorithm. Subsequently, the master dark frame is subtracted from the Pre-run, Run, and Post-run phases to eliminate fixed-pattern sensor noise.

- **Spatial Registration and Alignment:** To accurately track and compensate for global camera shift and mechanically induced vibrations, this module employs an up-sampled cross-correlation algorithm within a user-defined region of interest (ROI). Subsequent images are registered to the reference image and fiducial marker positions with sub-pixel accuracy using a piecewise affine warping projection.

- **Temporal Drift Correction:** This module compensates for low-frequency temporal drift, typically induced by the thermal stabilization and slight intensity degradation of the excitation LEDs over extended periods. Five distinct reference locations are selected across each phase to locally analyze and numerically correct this drift.

- **Normalization, Calibration, and Scaling:** This step calculates the normalized luminescent intensity ratio. The raw intensity counts of each Run image are divided by the temporally averaged Pre-run or Post-run reference image. A subsequent physical calibration integrates the synchronous temperature data acquired by the discrete Pt1000 sensors, mapping the normalized pixel intensities to absolute physical temperatures.

- **Masking:** This algorithm automatically isolates physical fiducial markers (e.g., painted tracking dots) within the field of view. It utilizes a combination of dark thresholding, Gaussian smoothing (σ), and a spread threshold to robustly segment the markers. Identified marker pixels are replaced with a uniform fill value (e.g., '1') to prevent them from corrupting subsequent algorithmic evaluations, such as spatial filtering or SPOD.

- **Spatial Filtering:** This module provides a suite of standard two-dimensional convolution operators (Mean, Median, Gaussian, Sobel, and Laplacian) utilized during various intermediate post-processing stages to smooth noise or enhance gradients.

- **Robust Principal Component Analysis (RPCA), Candès et al. (2011):** The image sequence is decomposed into two distinct matrices using the Alternating Direction Method of Multipliers (ADMM), Boyd et al. (2011). The resulting Low-Rank matrix captures the stationary background and smooth thermodynamic transients, while the Sparse matrix isolates rapidly moving tracer particles, high-frequency noise, or anomalies. The standard RPCA formulation is modified here to utilize Randomized Singular Value Decomposition (rSVD) for extracting the primary principal components, significantly accelerating the computational processing time.

- **Spectral Proper Orthogonal Decomposition (SPOD), Towne et al. (2018):** This module performs frequency-based modal analysis using overlapping Fast Fourier Transform (FFT) windows (typically utilizing a window size of 256 frames with a 50% overlap). This decompo-

sition extracts the dominant spatial structures (modes) that oscillate at specific, physically relevant frequencies within the flow field.

3.3. Inside-Out Particle Tracking Algorithm

To extract the near-wall particle kinematics from the internal camera setup, a custom two-dimensional particle tracking algorithm is applied directly to the image sequences. The tracking pipeline consists of the following sequential steps:

1. **Image Initialization:** The tracking algorithm does not operate on raw camera frames; instead, it utilizes the normalized ratio images generated during the TSP processing phase. Utilizing these ratio images is highly advantageous because the division by the pre-run reference frame inherently corrects for any spatial non-uniformity in the LED excitation field, ensuring the silhouetted particles are distinctly resolved against the luminescent background.
2. **Global Normalization:** The entire ratio-image stack undergoes a global intensity normalization to ensure uniform contrast across the full temporal sequence.
3. **Spatial Filtering:** A standard two-dimensional Gaussian filter is applied to each individual frame to mitigate high-frequency pixel noise and smooth the particle boundaries.
4. **Particle Detection:** Particle identification is achieved via a binary thresholding and blob-detection algorithm. To robustly reject spurious noise and sensor artifacts, a connected-component spatial filter is enforced, requiring that a valid particle must occupy a continuous region strictly greater than 8 pixels.
5. **Sub-Pixel Localization:** The exact spatial coordinates of each validated particle are determined by calculating its intensity-weighted centroid, yielding sub-pixel localization accuracy.
6. **Trajectory Linking:** Temporal linking of the discrete particle centroids into continuous paths is executed using a nearest-neighbor Greedy algorithm. This kinematic linking consists of three sub-steps:
   (a) All current detections are cross-referenced against the last known coordinates of active particle tracks.
   (b) For each established track, the algorithm searches for the closest available detection in the subsequent frame. This proximity-based matching is highly reliable due to the relatively low particle seeding density within the specific near-wall optical plane. To prevent erroneous linking, candidate particles are strictly required to fall within a predefined maximum search radius relative to their predecessor.

(c) Trajectory gap-closing (to bridge short instances of particle occlusion or missed detections) and final kinematic plausibility validations are subsequently performed via manual supervision.

7. **Coordinate Transformation:** Finally, the contiguous two-dimensional pixel trajectories are mathematically projected onto the physical cylindrical coordinate system utilizing the spatial calibration mapping.

For future inside-out tracking algorithm, a sparse matrix S from RPCA will be used instead of non-filtered ratios.

4. Results

4.1. TSP Temperature Field Extraction

The initial TSP post-processing and temperature field extraction are performed directly on the two-dimensional image sequences. Within this raw sensor space, the primary fluid flow is oriented from right to left. However, following the three-dimensional surface projection and mapping onto the unwrapped cylindrical coordinate system, the spatial data is reoriented to depict the flow moving from left to right.

To illustrate this pipeline, an exemplary measurement sequence is presented, showcasing the distinct stages of the post-processing procedure. These specific sample images were acquired utilizing a reduced spatial Region of Interest (ROI) on the internal camera sensor. Restricting the sensor ROI enabled a significant increase in the acquisition frame rate, thereby providing the enhanced temporal resolution strictly required to perform high-frequency spectral evaluations (such as SPOD) on the transient surface temperature fields.

Figure 5a displays a cropped region of the TSP field following initial spatial alignment and the calculation of the luminescent intensity ratio (the Run image divided by the Reference image). As mentioned, the flow is oriented from right to left and the data is aquired at sub critical conditions of 1 m/s and correspondin Reynolds number of In this normalized raw state, both the underlying surface temperature distribution and the discrete, illuminated tracer particles are clearly visible. By applying the modified RPCA algorithm, the image sequence is mathematically decomposed into a sparse matrix (S) and a low-rank matrix (L). As shown in Fig. 5b and Fig. 5c, this decomposition effectively separates the high-frequency particle signatures from the low-frequency thermodynamic background, allowing the kinematic and thermal data streams to be processed independently in all subsequent analysis stages. Since the flow is from right to left and we divided Run images by Reference images, the warmer region on the surface appear darker and colder regions appear brighter. Distinctly visible is also the laminar separation location identified by the dark-"warm" vertical line and subsequent flow inside the separated region.

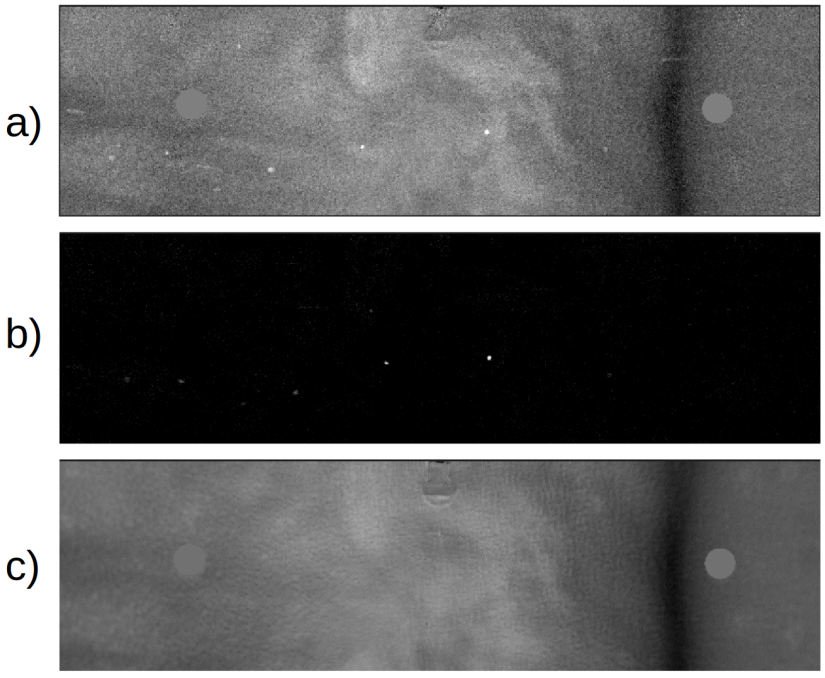


Figure 5. Decomposition of the internal TSP measurement images via RPCA: a) original cropped ratio image containing both thermodynamic and kinematic signatures; b) sparse matrix (S) isolating the high-frequency near-wall tracer particles; and c) low-rank matrix (L) representing the reconstructed, noise-filtered surface temperature (flow from the right).

Proper Orthogonal Decomposition (POD) is performed on the reconstructed low-rank matrix (L). Figure 6 illustrates the fractional energy content captured by each computed mode. Notably, over 95% of the total dataset variance is contained within the first 20 modes. Consequently, a low-order reconstruction utilizing only these leading 20 modes is highly effective; it sufficiently captures the dominant thermodynamic structures while systematically rejecting the higher-order, low-energy modes that primarily consist of residual image noise.

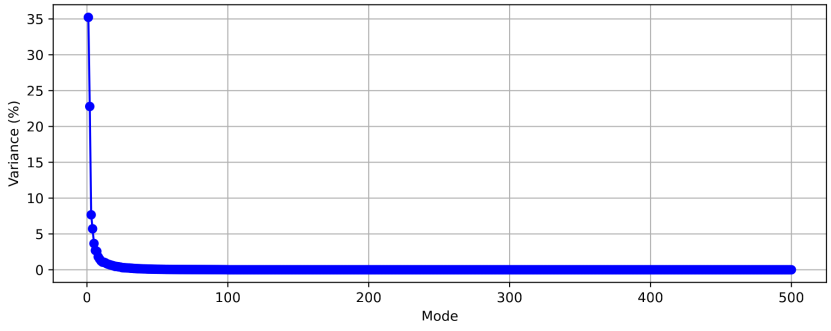


Figure 6. Energy distribution across the computed POD modes. Over 95% of the total spatial variance is captured within the first 20 modes, demonstrating the efficacy of truncating the low-order reconstruction at this threshold to filter residual noise.

To evaluate the spectral characteristics of the transient temperature field, Spectral Proper Orthogonal Decomposition (SPOD) is performed on the reconstructed low-rank dataset. Figure 7

presents the resulting SPOD energy spectrum. The leading spatial modes extracted at three distinct peak frequencies—2 Hz, 3.9 Hz, and 19.5 Hz—are illustrated in Fig. 8. These specific spectral peaks are physically associated with the dominant dynamics of the near-wall flow field and the coupled fluid-solid thermal interactions. Conversely, spectral energy observed at frequencies exceeding 20 Hz is primarily attributed to residual image noise and high-frequency structural microvibrations of the cylinder model.

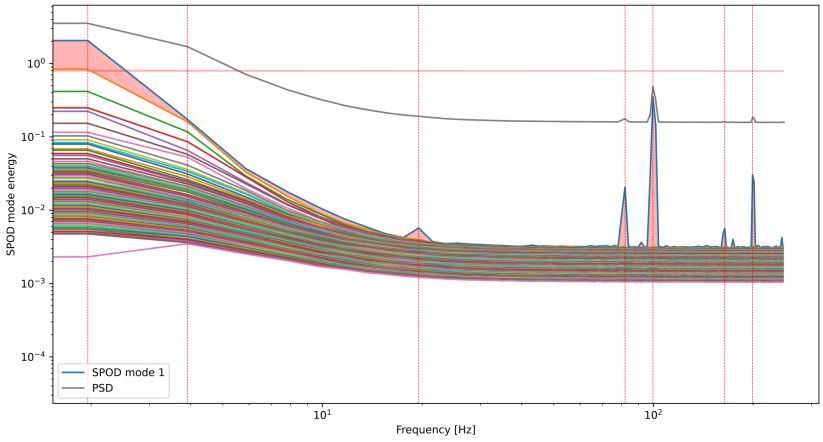


Figure 7. SPOD energy spectrum derived from the reconstructed surface temperature field, highlighting the dominant dynamic frequencies.

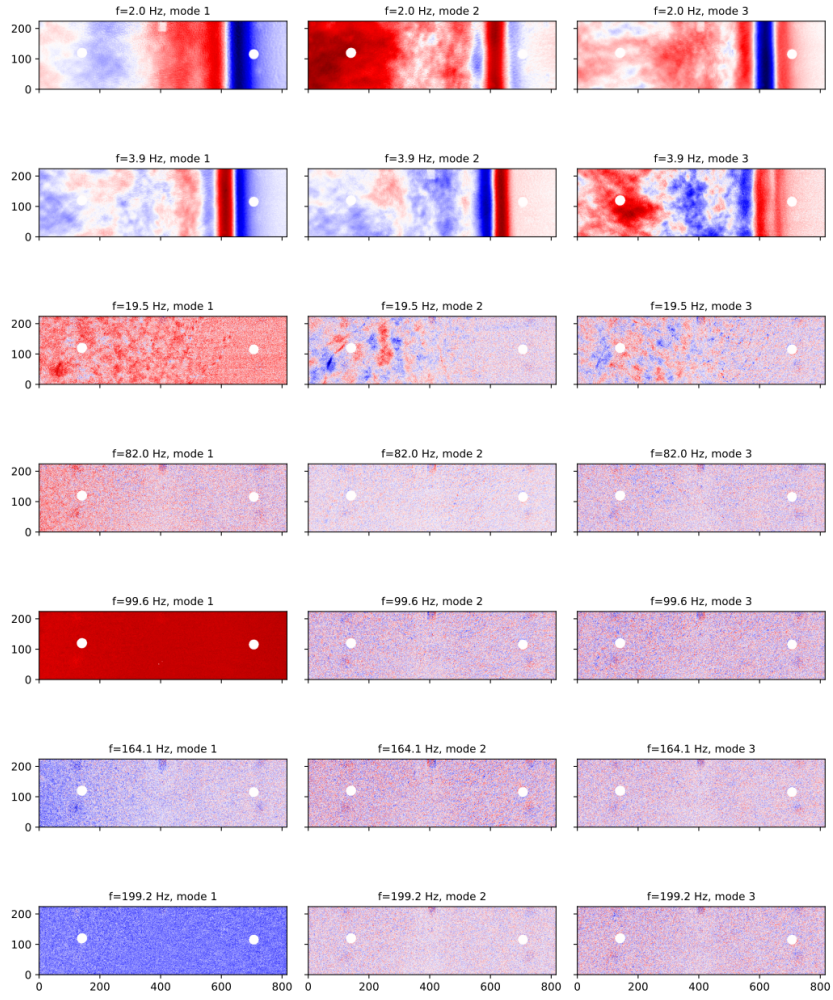


Figure 8. Spatial structures of the leading SPOD modes corresponding to the distinct spectral peaks at 2 Hz, 3.9 Hz, and 19.5 Hz.

Finally, the temperature gradient variation across the image can be extracted and wall-shear-stress calculated. This step is not part of this conference publication.

4.2. 3D Flow Field and Data Fusion

Because the dual-optical diagnostic system achieves high spatiotemporal resolution, fine-scale coherent structures within the separated wake are successfully captured alongside the broader, macroscopic dynamics of the time-variant boundary layer separation.

Figures 9 and 10 illustrate two instantaneous snapshots of the fused dataset, showcasing the external 3D-PTV flow field trajectories perfectly synchronized with the underlying projected surface temperature fields. Corresponding to these three-dimensional projections, Figures 11 and 12 display the two-dimensional, unwrapped TSP temperature maps. In these planar representations, the freestream flow is oriented from left to right, encompassing the entire imaged spatial domain. Consistent with the established intensity colormap, warmer surface regions are rendered in dark

tones, whereas colder regions appear white. Across these sequential frames, the unsteady, oscillatory movement of the primary separation region is clearly observable.

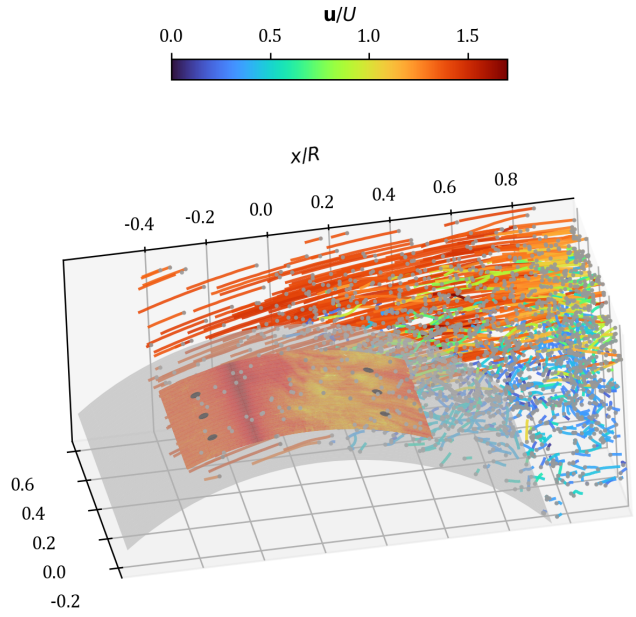


Figure 9. Time- and space-synchronized particle tracks (3D-PTV) and TSP intensity ratio on the cylinder surface. Phase: $T^* = 0$.

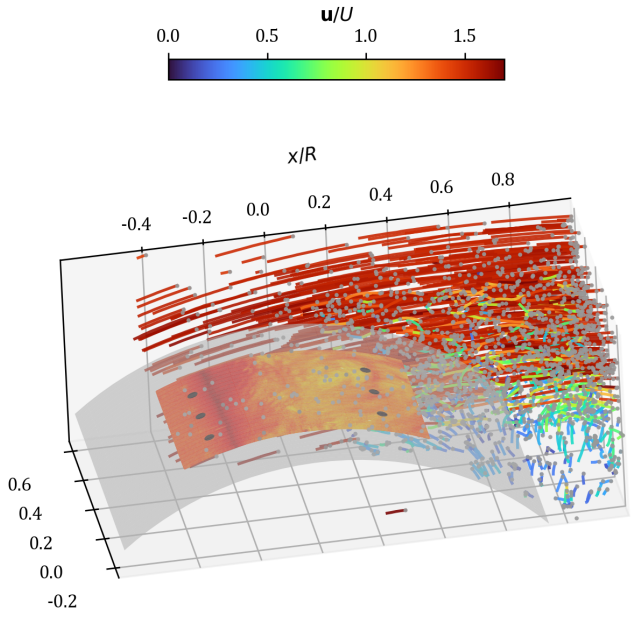


Figure 10. Time- and space-synchronized particle tracks (3D-PTV) and TSP intensity ratio on the cylinder surface. Phase: $T^* = \pi/2$.

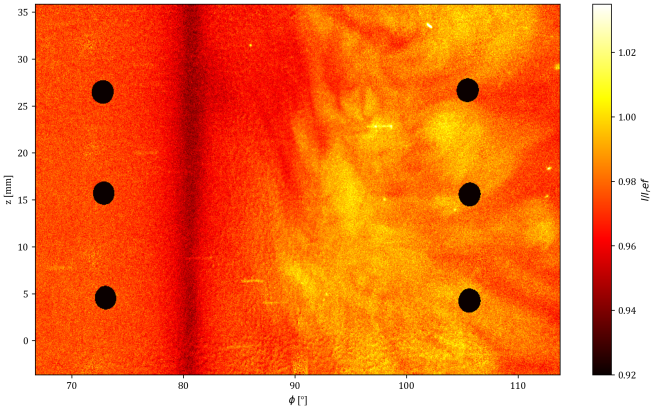


Figure 11. Unwrapped TSP intensity ratio at the most backward separation location ($\phi_s = 81°$). Phase: $T^* = 0$.

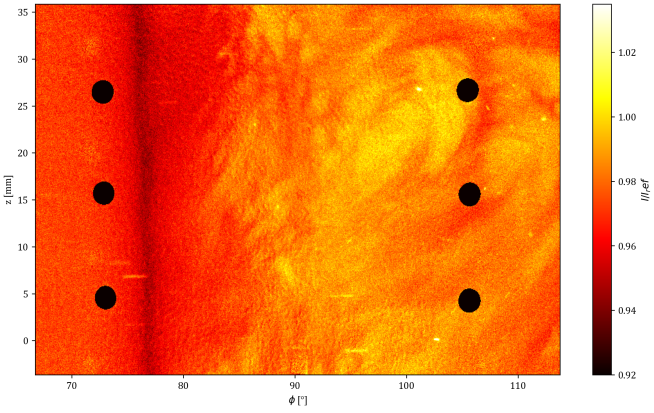


Figure 12. Unwrapped TSP intensity ratio at the most forward separation location ($\phi_s = 76°$). Phase: $T^* = \pi/2$.

Figure 13 presents an overlay of discrete near-wall particle trajectories onto the instantaneous TSP fields. The underlying thermodynamic footprint is visualized as a field of normalized luminescent intensity (I/I_{ref}). The color-coding along each individual trajectory represents the localized particle intensity, normalized by the dynamic intensity range of that specific track ($I_{tr,\max} - I_{tr,\min}$). To clarify the kinematic history, a circular marker denotes the terminal end of the trajectory, indicating the

overall direction of motion, while a cross marker pinpoints the exact spatial coordinates of the particle at the specific time-step of the underlying TSP frame. Physically, these specific tracer particles are entrained in the reverse flow, traveling upstream toward the origin of the primary separation region before experiencing a subsequent flow reversal.

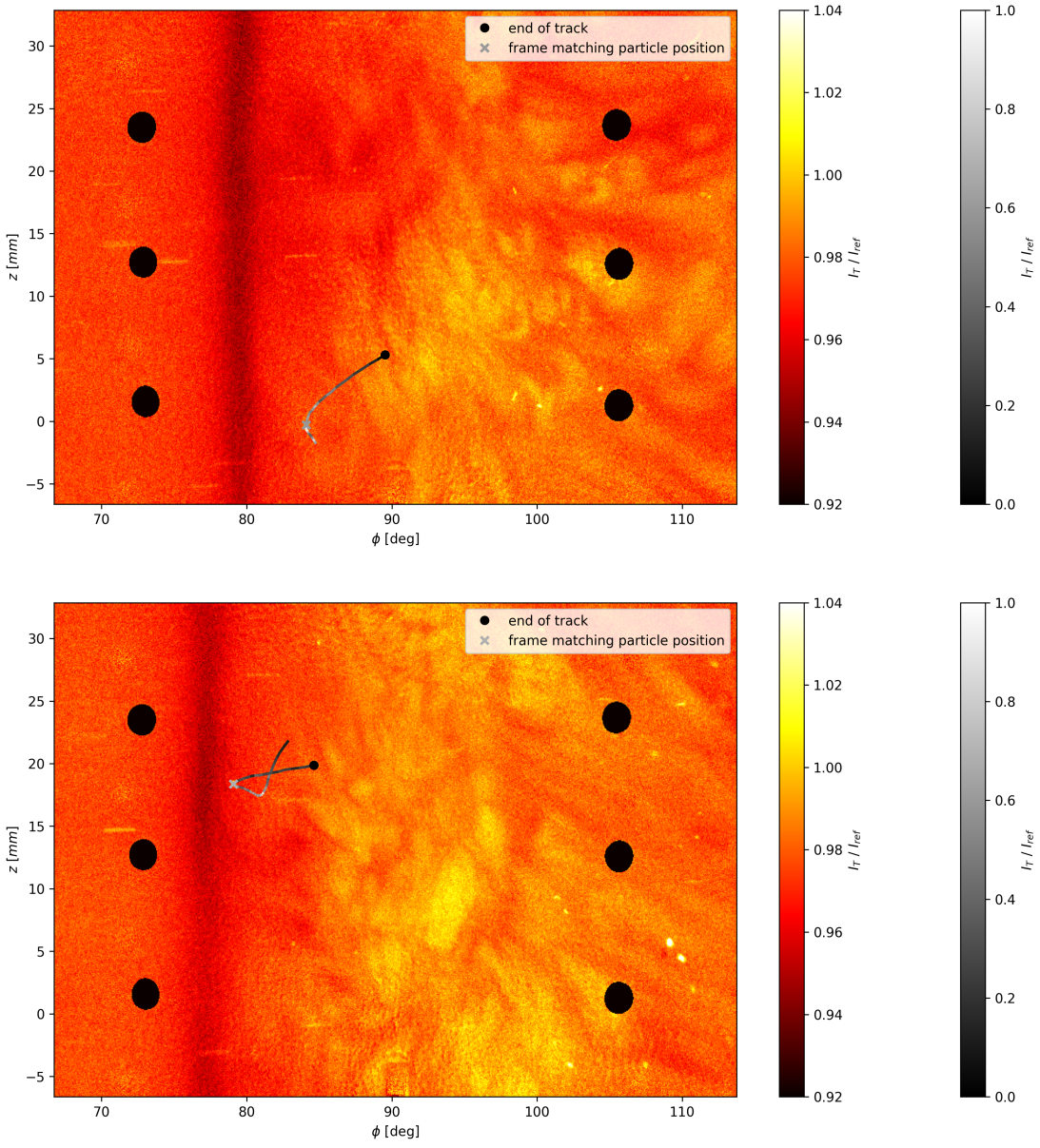


Figure 13. Overlay of normalized particle track intensities and the instantaneous TSP intensity ratio (I/I_{ref}) for two distinct near-wall trajectories at a subcritical Reynolds number of $Re_D = 1.9 \times 10^5$.

When compared to the theoretical kinematics illustrated in Fig. 1, the tracer particles presented in Fig. 13 exhibit clear evidence of a Lagrangian ejection event. Due to the relatively sparse spatial density of the reconstructed tracks, it is not currently feasible to resolve the full continuous material manifold of the separating fluid. Nevertheless, the discrete instances of individual particles being repelled from the wall are unambiguously captured. In future measurement campaigns, uti-

lizing a higher seeding density coupled with smaller tracer particles will increase the probability of capturing multiple tracers simultaneously near the critical separation locations. This refinement will enable a quantitative evaluation of the evolving material manifold, thereby establishing a direct, physical correlation between the fluid ejection events and the underlying surface temperature measurements—particularly the local temperature gradient fields.

5. Conclusions and Outlook

This study successfully demonstrates the implementation of a novel, model-integrated and back-illuminated temperature-sensitive paint (TSP) diagnostic system, fundamentally enabling the simultaneous measurement of continuous surface thermodynamics and discrete Lagrangian fluid kinematics. By decoupling the optical measurement train from external facility constraints via a transparent, internally heated cylinder model, critical experimental limitations such as optical distortion, restricted viewing angles, and particle shadowing were completely circumvented.

The advanced computational data processing pipeline, utilizing a modified Robust Principal Component Analysis (RPCA) algorithm, proved highly effective in decomposing the raw sensor data. It successfully isolated the sparse, high-frequency signatures of near-wall tracer particles from the low-rank, noise-filtered surface temperature distributions. Subsequent spectral analysis via SPOD identified distinct dynamic frequencies (e.g., $2\,\mathrm{Hz}$, $3.9\,\mathrm{Hz}$, and $19.5\,\mathrm{Hz}$) characterizing the separation bubble and boundary layer interactions. Crucially, the precise spatial and temporal fusion of the internal two-dimensional TSP fields with the external volumetric 3D-PTV measurements provided an unprecedented, unobstructed view of the separating flow topology. The direct overlay of discrete near-wall particle trajectories onto the transient temperature fields yielded clear experimental evidence of Lagrangian fluid ejection events, corroborating theoretical models of unsteady separation.

Future measurement campaigns will focus on higher Reynolds numbers above critical regime. Furthermore, two primary objectives to fully exploit this diagnostic architecture will be persude. First, the experimental configuration will be refined to utilize smaller tracer particles (nominally $20\,\mu\mathrm{m}$) coupled with a significantly higher spatial seeding density. This enhancement will mitigate spatial averaging within high-shear regions and allow for the resolution of the continuous material manifold of the separating fluid, bridging the gap between discrete particle tracking and continuous topological evolution. Second, the reconstructed, high-fidelity transient temperature fields will be processed utilizing the established optical flow (OF) methodology to extract the instantaneous wall-shear-stress and divergence fields. By directly linking these derived surface shear topologies with the simultaneously observed three-dimensional particle ejection events, the ultimate objective is to provide a rigorous, quantitative experimental validation of the Lagrangian Repulsion Rate criterion in highly unsteady, sub- and supercritical flow regimes.

Acknowledgments

ONR Grant N62909-24-1-2115

Nomenclature

Roman Symbols

D	Cylinder outer diameter [m]
F	Unsteady thermal source term
I	Luminescent emission intensity
k	Thermal conductivity [W/(m K)]
L	Low-rank matrix component (RPCA)
Re_D	Reynolds number based on cylinder diameter
Ri	Richardson number
S	Sparse matrix component (RPCA)
T	Temperature [K]
T^*	Phase angle
t	Time [s]
u, v, w	Velocity components aligned with x, y, z coordinates [m/s]
x, y, z	Cartesian coordinates (streamwise, wall-normal, spanwise) [m]
y^+	Non-dimensional wall distance

Greek Symbols

α_{th}	Thermal diffusivity [m^2/s]
μ	Dynamic viscosity [Pa s]
$h\nu_{ex}$	Excitation photon energy
Φ	Quantum efficiency
ϕ_s	Angular separation location [°]
ρ	Lagrangian repulsion rate [1/s]
$\dot{\rho}$	Rate of change of repulsion rate [1/s^2]
τ_w	Wall shear stress vector [Pa]
τ_x, τ_z	Streamwise and spanwise wall shear stress components [Pa]

Subscripts

∞	Freestream condition
nr	Non-radiative decay
r	Radiative decay

ref	Reference state
tr	Particle track
w	Wall condition

REFERENCES

Boyd, S. P., Parikh, N., Chu, E., Peleato, B., & Eckstein, J. (2011). Distributed optimization and statistical learning via the alternating direction method of multipliers. *Foundations and Trends® in Machine Learning*, *3*(1), 1–122. doi:

Candès, E. J., Li, X., Ma, Y., & Wright, J. (2011). Robust principal component analysis? *Journal of the ACM (JACM)*, *58*(3), 1–37. doi:

Haller, G. (2015). Lagrangian coherent structures. *Annual Review of Fluid Mechanics*, *47*, 137-162. Retrieved from https://api.semanticscholar.org/CorpusID:122894798

Horn, B., & Schunck, B. (1981). Determining optical flow. *Artificial Intelligence*, *17*(1), 185-203. Retrieved from https://www.sciencedirect.com/science/article/pii/0004370281900242 doi:

Liu, T., Sullivan, J. P., Asai, K., Klein, C., & Egami, Y. (2021). *Pressure and temperature sensitive paints*. Springer Nature Switzerland AG.

Liu, T., & Woodiga, S. (2011). Feasibility of global skin friction diagnostics using temperature sensitive paint. *Measurement Science and Technology*, *22*(11), 115402.

Miozzi, M., Capone, A., Di Felice, F., Klein, C., & Liu, T. (2016). Global and local skin friction diagnostics from tsp surface patterns on an underwater cylinder in crossflow. *Physics of Fluids*, *28*(12), 124101.

Sadr, M., & Vétel, J. (2024). Turbulent separation detection based on a lagrangian approach. In *Proceedings of the 13th international symposium on turbulence and shear flow phenomena (tsfp13)* (p. Paper 80). Retrieved from https://www.tsfp-conference.org/proceedings/2023/80.pdf

Sears, W. R., & Telionis, D. P. (1975). Boundary-layer separation in unsteady flow. *SIAM Journal on Applied Mathematics*, *28*(1), 215-235. doi:

Serra, M., Vétel, J., & Haller, G. (2018). Exact theory of material spike formation in flow separation. *Journal of Fluid Mechanics*, *845*, 51–92. doi:

Towne, A., Schmidt, O. T., & Colonius, T. (2018). Spectral proper orthogonal decomposition and its relationship to dynamic mode decomposition and resolvent analysis. *Journal of Fluid Mechanics*, *847*, 821–867. doi: